

Topological nodal-line semimetals in ferromagnetic rare-earth-metal monohalides

Simin Nie^{1,*}, Hongming Weng^{2,3}, and Fritz B. Prinz^{1,4}

¹*Department of Materials Science and Engineering,
Stanford University, Stanford, California 94305, USA*

²*Beijing National Laboratory for Condensed Matter Physics,
and Institute of Physics, Chinese Academy of Sciences, Beijing 100190, China*

³*Collaborative Innovation Center of Quantum Matter, Beijing 100190, China and*

⁴*Department of Mechanical Engineering, Stanford University, Stanford, California 94305, USA*

(Dated: January 24, 2019)

Topological semimetals, extending the topological classification from insulators to metals, have greatly enriched our understanding of topological states in condensed matter. This is particularly true for topological nodal-line semimetals (TNLSs). In the present paper, we identify layered materials as promising candidates for hosting TNLSs. Based on first-principles calculations and effective model analysis, we propose that layered ferromagnetic rare-earth-metal monohalides LnX (Ln=La, Gd; X=Cl, Br) exhibit long pursued topological phases. Specifically, single-layer LaX and single-layer GdX are ideal two-dimensional (2D) Weyl semimetals and large-gap 2D quantum anomalous Hall insulators (QAHIs), with band gaps up to 61 meV, respectively. In addition, 3D LaX and 3D GdX are TNLSs with a pair of mirror-symmetry protected nodal lines and 3D QAHIs, respectively. The nodal lines in 3D LaX extending through the whole Brillouin zone (BZ) are fairly robust against strong spin-orbit coupling (SOC) and located close to the Fermi level, providing a novel platform toward exploring the exotic properties in nodal-line fermions as well as related device designs.

I. INTRODUCTION

Nodal-line fermions¹⁻³, a new type of fermions beyond Dirac⁴⁻⁶ and Weyl fermions⁷⁻⁹, have attracted ever-increasing interest in the field of condensed matter physics due to the absence of an elementary particle counterpart in high-energy physics. Topological materials hosting nodal-line fermions (known as TNLSs) can be driven into various topological states, such as Weyl semimetals^{10,11}, Dirac semimetals^{12,13}, topological insulators^{14,15} and QAHIs^{16,17}, by including SOC effect or breaking certain symmetry (for example mirror symmetry). In TNLSs, the highest valence and the lowest conduction bands touch each other along 1D symmetry-protected lines in the momentum space of the bulk, which can take many different forms, such as closed lines inside the BZ¹⁸, extended lines traversing the BZ¹⁹, or nodal chain consisting of connected lines²⁰ *etc.* The nodal lines carrying quantized π -Berry phase are protected by crystal symmetry or the coexistence of time-reversal and inversion symmetries, and always lead to nearly flat drumhead-like states with infinite density of states (DOS) on the boundary. These unique characteristics generate some exotic properties in TNLSs: high-temperature surface superconductivity²¹⁻²³, unique Landau energy level²⁴, and special long-range Coulomb interactions²⁵, *etc.*

Although there has been great progress in theoretical prediction of TNLSs in real materials with small SOC interaction²⁶⁻³⁴, the nontrivial nodal lines have been only confirmed in pure alkali earth metals by photoemission spectroscopy experiments³⁵. Owing to the fact that the non-negligible SOC can always gap out the nodal lines protected by inversion and time reversal symmetries, almost all candidates evolve into either topological insu-

lators or Dirac semimetals. Another route to TNLSs is to introduce the crystal symmetry (for example, mirror symmetry or glide-mirror symmetry). However, very few materials are predicted to host nodal lines protected by the crystal symmetry^{36,37}, which are robust against SOC. What's worse, most nodal lines are far away from the Fermi level and not formed by band touching of the highest valence band and the lowest conduction band^{38,39}. To the best of our knowledge, the signature of the existence of drumhead surface states is only observed in nonmagnetic PbTaSe₂³⁷, in which the existence of trivial Fermi pockets and some accidental nodal lines results in very complicated spectroscopic and transport properties. In fact, more research is needed regarding the illustration of the direct relationship between the symmetry-protected nodal lines and the drumhead surface states because of such complicated band structure.

The revealed TNLSs so far are extremely limited to nonmagnetic materials despite the discovery of various topological nontrivial states in magnetic materials⁴⁰⁻⁴³. It is well known that magnetic order can significantly modify the electronic structure and may give rise to the nontrivial nodal lines. Considering that the nodal lines in nonmagnetic materials can always be gapped out under sufficiently large SOC even in PbTaSe₂, the realization of TNLSs in magnetic systems would be much more desirable and significant. Here, we find that layered materials are very likely to host spinful nodal lines. Guided by this insight, we show that some long pursued topological phases can be achieved in layered ferromagnetic LnX. The interlayer binding energies of 3D LnX are weaker than that of graphite, which means it may be able to make single-layer LnX in a very simple and efficient way. Our calculations show that single-layer LaX are ideal 2D Weyl semimetals with Weyl nodes located close to the

Fermi level, and single-layer GdX are promising large-gap 2D QAHI with band gaps up to 61 meV. More interestingly, 3D LaX are TNLSs with a pair of spinful nodal lines nearly at the Fermi level, and 3D GdX are rare 3D QAHI⁴⁴. In contrast to conventional nodal lines, the spinful nodal lines with quantized π -Berry phase are protected by mirror symmetry with respect to the xoz plane, and can only be removed when they meet in the momentum space⁴⁵. The topological phases in LnX, especially the TNLSs in 3D LaX, pave a new way for studying the corresponding exotic properties in condensed matter systems.

II. CALCULATION METHODS

The full-potential linearized augmented plane-wave method implemented in WIEN2K package⁴⁶ is employed to perform the first-principles calculations, which are cross-checked with the projector augmented wave method implemented in Vienna ab initio simulation package^{47,48}. The exchange and correlation potential is treated within the local-density approximation (LDA) of Perdew- and Wang-type⁴⁹. SOC is taken into account as a second variational step self-consistently. The k -point grids of the BZ with $18 \times 18 \times 18$ and $20 \times 20 \times 1$ are used in the self-consistent calculations of 3D LnX and single-layer LnX, respectively. The radii of the muffin-tin sphere R_{MT} in the calculations are 2.5 bohrs for La, Gd, and Br and 2.39 bohrs for Cl, respectively. The LDA+U method⁵⁰ is carried out to properly treat the correlation effect in LnX with $U = 5$ eV and $U = 6$ eV for d orbitals of La and f orbitals of Gd, respectively. The s and d orbitals of Ln are used to construct the maximally localized Wannier functions (MLWFs)⁵¹, which are then used to calculate the boundary states by an iterative method⁵²⁻⁵⁴.

The strength of van der Waals forces holding the layers of bulk can be described by the interlayer binding energy, which is defined as

$$E_b = -\frac{E_{\text{bulk}} - N \cdot E_{\text{layer}}}{N \times S_{\text{layer}}}$$

where E_{bulk} and E_{layer} are the total energies of a bulk unit cell and a single-layer unit cell, respectively. N is the number of layers in the bulk unit cell. S_{layer} is the area of the single-layer unit cell.

The Berry phase of a ring (ℓ) piercing the nodal line (shown as black lines in Fig. 2(e)) is quantized to be π and can be defined as

$$\phi_\ell = \oint_\ell \mathbf{A}(\mathbf{k}) \cdot d\mathbf{k}$$

where $\mathbf{A}(\mathbf{k}) = -i \sum_{n \in \text{occ.}} \langle u_n(\mathbf{k}) | \partial_{\mathbf{k}} | u_n(\mathbf{k}) \rangle$ is the Abelian Berry connection and $|u_n(\mathbf{k})\rangle$ are the Bloch states. The Berry phase is defined in terms of modulo 2π .

III. RESULTS AND DISCUSSION

A. Evolution of band crossings from 2D to 3D systems

Both the theoretical proposal^{55,56} and the experimental realization⁵⁷ of topological nontrivial properties are based on 2D materials (2D topological insulators) at the beginning, and 2D topological insulators have been generalized to 3D topological insulators very soon⁵⁸, which are classified into 3D strong topological insulators and 3D weak topological insulators according to the interlayer coupling strength. Similar to the situation in the topological insulators protected by time reversal symmetry, the nodal lines can also be found in the 3D materials constructed by stacking the 2D materials with twofold-degenerate band crossings (called Weyl nodes). Although H. Nielsen and M. Ninomiya only shown that the no-go theorem holds on 1D and 3D lattices^{59,60}, the theorem is also applicable to 2D lattice with specified symmetry⁶¹⁻⁶³, such as time reversal symmetry. Contrary to the fairly robust Weyl nodes in 3D materials, the Weyl nodes in 2D materials are unstable. Thus, additional symmetry is needed to guarantee its existence, such as mirror symmetry. Therefore, for simplicity, we only consider a pair of Weyl nodes in a 2D material with mirror symmetry \hat{M}_y , as shown in Fig. 1(e). Then, the 2D Weyl semimetal is stacked into a 3D layered material, which can be grouped into three different nontrivial semimetal classes depending on the interlayer coupling strength and the symmetry. For the symmetry-protected Weyl nodes stacked along a line preserving the symmetry, the Weyl nodes can evolve into two different classes (see more details in the Appendix A): Class1, two nodal loops extending through the BZ for the layered materials with weak interlayer coupling; Class2, closed loops or accidental nodal chain for the layered materials with strong interlayer coupling. On the other hand, if the symmetry is broken on the stacking line, the layered material may become a 3D Weyl semimetal, which belongs to Class3. Therefore, in consideration of the robust existence of nodal lines in layered materials, it is much promising to search for the TNLSs in this kind of material with proper symmetry.

B. Crystal structure, magnetic configurations, and Nodal lines

Guided by this idea, the nontrivial nodal lines are found in a class of topological materials LnX. LnX are well-known layered materials and have been synthesized since the early 1980s^{64,65}. Experimentally, they all crystalline in the hexagonal layered structure with space group $R\bar{3}m$ (No. 166), as shown in Fig. 1(a). The basic building block of LnX is a tightly bound quadruple layer, which consists of two hexagonal rare-earth-metal (Ln) layers sandwiched between two hexagonal halogen

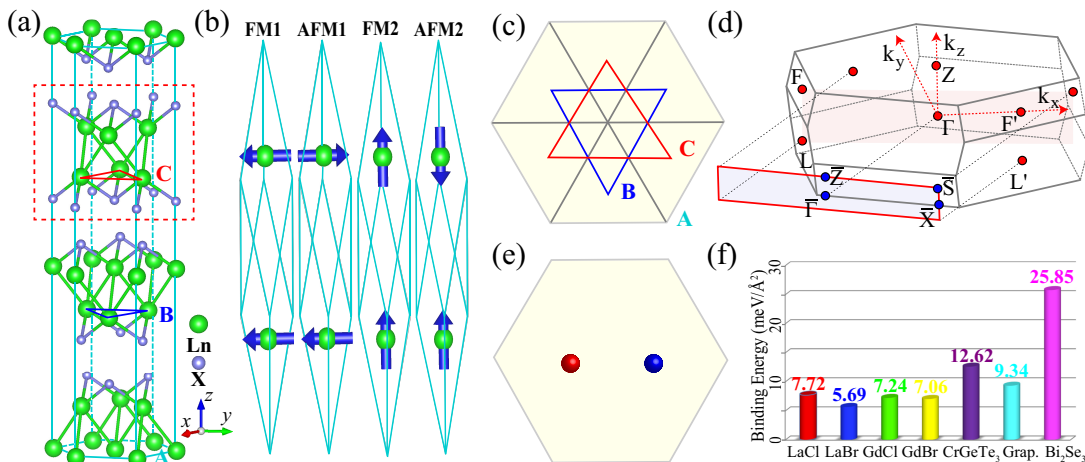


FIG. 1. (Color online) Crystal structure and topological phase evolution. (a) Crystal structure of 3D LnX. The green and light blue balls represent Ln and X, respectively. The quadruple layer is indicated by the red dashed line. (b) Schematics of four different collinear magnetic structures for LnX in the primitive cell. For simplicity, only Ln atoms are shown, while the nonmagnetic X atoms are omitted. (c) Top view of LnX. Each unit cell consists of three quadruple layers stacked in an ABC-type trilayer pattern along the z -direction. (d) The bulk BZ and the projected surface BZ for (010) surface of LnX. The grey plane indicates the xoz plane. (e) Schematic of a 2D BZ and the boundary paths used to calculate the Berry phases. (f, g) Schematics of 2D Weyl semimetal and 3D TNLS, respectively. (h) The interlayer binding energies of layered materials (LnX, CrGeTe₃, Graphite and Bi₂Se₃).

(X) layers in the sequence of X-Ln-Ln-X. The adjacent quadruple layers are stacked in an ABC-type trilayer pattern along the z -direction with much weak van der Waals (vdW) interaction, as shown in Fig. 1(c).

Given that the interlayer distance is very close to 10 Å, the interlayer binding strength of LnX should be much weaker than that of most layered compounds. We have calculated the interlayer binding energies of LnX as well as three well-established layered materials (graphite, Bi₂Se₃, and CrGeTe₃). The results are shown in Fig. 1(f), which are consistent with previous results⁶⁶ and cross-checked with vdW density functional (vdW-DF) calculations⁶⁷. It is easy to find that Bi₂Se₃ has the highest binding energy among these seven materials and the interlayer bonding of CrGeTe₃ is as weak as that of graphite, which is a main reason for the recent realization of 2D ferromagnetic CrGeTe₃⁶⁸. More interestingly, the interlayer coupling of LnX is even weaker than that of graphite, suggesting single-layer LnX can be easily produced by exfoliation methods.

Next, we consider the magnetic structure in LnX. Although magnetic structures and the transition temperatures of LnX have not been reported yet, it is reasonable to expect magnetic order in LnX due to the monovalent Ln. Due to the fact that the results of single-layer LnX are similar to that of 3D LnX, we only discuss the results of 3D LnX in the following (see more details in the Appendix B). Here, by using LDA+Hubbard U+SOC (LDA+U+SOC), we calculate the total energies of four different magnetic configurations for 3D LnX, including two ferromagnetic (FM1, FM2) and two antiferromagnetic (AFM1, AFM2) configurations shown in Fig. 1(b), and the converged total energies are summarized in Ta-

ble I. The results clearly show that both 3D LaX and 3D GdX prefer a ferromagnetic ground state, lowering the total energy in the range of dozens meV than the AFM configurations. More interestingly, 3D LaX and 3D GdX prefer FM1 with the spin aligned along the y -direction and FM2 with the spin aligned along the z -direction, respectively, in spite of the small energy difference between FM1 and FM2 (2.09/1.52 meV and 0.72/1.08 meV for 3D LaCl/3D LaBr and 3D GdCl/3D GdBr, respectively). In addition, we have checked the magneto-crystalline anisotropy energy within the xoy plane for LaX. The magneto-crystalline anisotropy energy is of the order of 0.0001 meV, indicating LaX are soft magnetic materials with an easy magnetization axis in the xoy plane. Experimentally, an external magnetic field can be used to realize the FM1 state and the topological semimetals in LaX. So we only focus the topological properties of LaX with FM1 state in the following discussion.

The point group for the nonmagnetic materials with space group $R\bar{3}m$ is the D_{3d} symmetry group, which has three generators: threefold rotational symmetry about the z -axis (\hat{C}_3^z), inversion symmetry (\hat{I}), and mirror symmetry with respect to the xoz plane (\hat{M}_y). For 3D LaX, the ferromagnetic order (FM1) breaks \hat{C}_3^z and the little group is reduced from D_{3d} to C_{2h} with generators \hat{I} and \hat{M}_y only. However, for 3D GdX, FM2 breaks \hat{M}_y and the little group becomes C_{3i} with generators \hat{I} and \hat{C}_3^z only. The FM ground states with different symmetries lead to different band structures and topological phases in LnX, as will be shown below.

Since LaBr has almost the same results as LaCl, we choose LaCl as an example in the following demonstra-

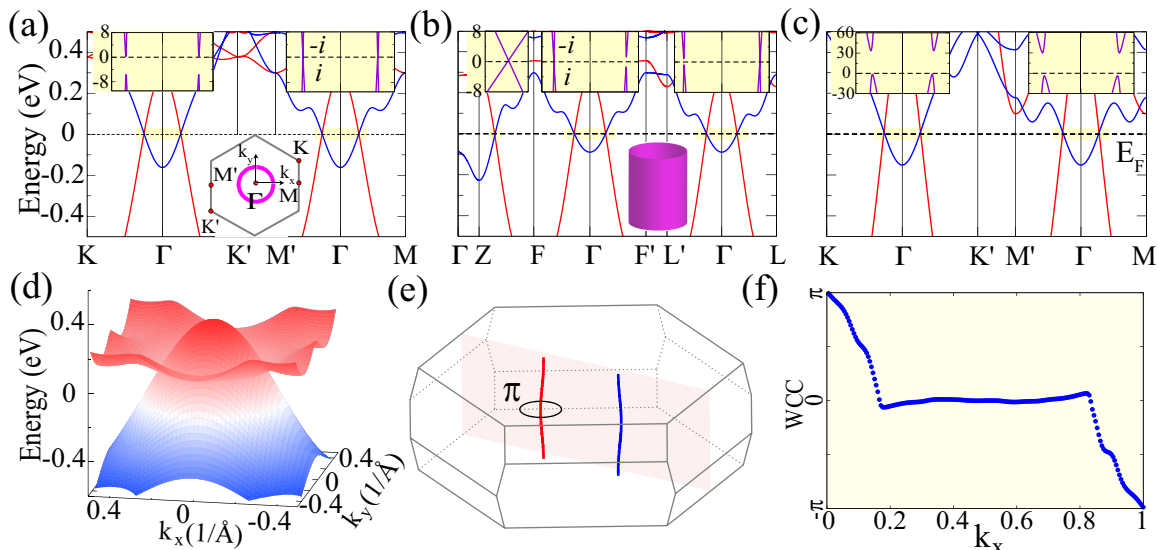


FIG. 2. (Color online) Electronic structures of LnX. (a, b, c) The LDA+U band structures of single-layer LaCl, 3D LaCl and single-layer GdCl, respectively. The red and blue lines represent spin-up and spin-down states, respectively. The upper insets show the zoom-in LDA+U+SOC band structures around the band crossing points. The lower insets of (a) and (b) show the schematics of the nodal line and cylinder, respectively. The eigenvalues of mirror symmetry \hat{M}_y are labeled. The energy unit of upper insets is meV instead of eV. (d) 3D band structure of 3D LaCl in the xoy plane without the consideration of SOC. (e) Two nodal lines of 3D LaCl are located in the xoz plane, which is indicated as grey plane. (f) The evolution of Wannier charge centers for single-layer GdCl.

tion. The calculated band structures of single-layer LaCl by LDA+U are shown in Fig. 2(a), which show a very deep band inversion at Γ point. When SOC is ignored, the band inversion results in a nodal line circled around Γ point, as shown in the lower inset of Fig. 2(a). The nodal line is mainly contributed by Ln $|d_{z^2}\rangle$, $|d_{x^2-y^2}\rangle$ and $|d_{xy}\rangle$ orbitals (see more details in the Appendix C). Then, when SOC is taken into consideration, the nodal line is gapped out, except the band crossings of k points on the $M - \Gamma - M'$ line, decaying into two Weyl nodes, as shown in the upper insets of Fig. 2(a). As discussed above, the ideal Weyl nodes in 2D LaCl with the nodes located close to the Fermi level may lead to nodal lines in 3D LaCl due to the extremely weak interlayer coupling. In order to confirm the speculation, we calculate the band structures of 3D LaCl, as shown in Fig. 2(b) and 2(d). Without the consideration of SOC, there is a cylinder centered around Γ point that originates from the nodal line of single-layer LaCl, as shown in the lower inset of Fig. 2(b). Considering SOC, the cylinder is gapped out everywhere except the band crossings of k points in the xoz plane (i.e., 3D LaCl belongs to the Class1), as shown in the upper insets of Fig. 2(b). The calculations of the eigenvalues of mirror symmetry \hat{M}_y indicate that the two crossing bands have opposite mirror eigenvalues $\pm i$, which means the nodal lines are protected by mirror symmetry \hat{M}_y . It is worth noting that the extended nodal lines in 3D LaCl always appear in pairs, as shown in Fig. 2(e), which is different from the conventional nodal lines. They can only be annihilated without breaking \hat{M}_y when

they meet in the momentum space.

C. $k \cdot p$ analysis and drumhead-like surface states

As discussed above, the little group at Γ point for 3D LaX is C_{2h} with generators \hat{I} and \hat{M}_y only. In the following, we can prove by a simple $k \cdot p$ analysis in the vicinity of Γ point that these two symmetries are enough to guarantee the existence of a pair of nodal lines around Γ point in 3D LaX. An effective low-energy 2×2 model capturing the nodal lines can be in general written in the form

$$H^\Gamma(\mathbf{k}) = \sum_{i=x,y,z} d_i(\mathbf{k}) \sigma_i \quad (1)$$

where σ_i are three Pauli matrices; $d_i(\mathbf{k})$ are real functions; $\mathbf{k} = (k_x, k_y, k_z)$ is the momentum vector relative to Γ point. The identity matrix σ_0 just shifts the Fermi level and is ignored in Eq. 1. The two crossing bands around Γ point in 3D LaX have the same parity, which indicates that the inversion symmetry \hat{I} is represented by $\hat{I} = \sigma_0$. Then, the inversion symmetry requires that

$$\hat{I} H^\Gamma(\mathbf{k}) \hat{I}^{-1} = H^\Gamma(-\mathbf{k}) \quad (2)$$

which means $d_i(\mathbf{k})$ are even functions of \mathbf{k} and can be up to the second order of \mathbf{k} generally written as

$$d_i(\mathbf{k}) = c_0^i + c_1^i k_x^2 + c_2^i k_y^2 + c_3^i k_z^2 + c_4^i k_x k_y + c_5^i k_y k_z + c_6^i k_x k_z \quad (3)$$

where c_n^i , $n = 0, \dots, 6$, are parameters characterizing the band structure. In addition, the two crossing bands have opposite mirror eigenvalues, which means the mirror symmetry \hat{M}_y can be represented by $\hat{M}_y = \sigma_z$. Therefore, another constraint on $H^\Gamma(\mathbf{k})$ placed by the mirror symmetry is

$$\sigma_z H^\Gamma(k_x, k_y, k_z) \sigma_z = H^\Gamma(k_x, -k_y, k_z) \quad (4)$$

which leads to

$$d_{x/y}(k_x, k_y, k_z) = -d_{x/y}(k_x, -k_y, k_z) \quad (5)$$

$$d_z(k_x, k_y, k_z) = d_z(k_x, -k_y, k_z) \quad (6)$$

Considering the constraints on $d_i(\mathbf{k})$ (Eq. 3, 5, and 6), we can get

$$d_{x,y}(k_x, k_y, k_z) = c_4^{x,y} k_x k_y + c_5^{x,y} k_y k_z \quad (7)$$

$$d_z(k_x, k_y, k_z) = c_0^z + c_1^z k_x^2 + c_2^z k_y^2 + c_3^z k_z^2 + c_6^z k_x k_z \quad (8)$$

Then, we discuss the constraints on c_n^i and the emergence of nodal lines due to the band inversion at Γ point in 3D LaX. It is easy to find that the band inversion requires $c_0^z < 0$. In addition, the band order along the k_x direction shows a transition from inverted to normal order, which indicates $c_1^z > 0$. However, the two bands are always inverted along the k_z direction, which indicates $c_3^z < 0$. The signs of c_n^z are important to give rise to nodal lines, which can be easily proved by following simple discussion. The appearance of the band crossing points in the $k_y = 0$ plane requires

$$c_0^z + c_1^z k_x^2 + c_3^z k_z^2 + c_6^z k_x k_z = 0 \quad (9)$$

Given $4 * c_1^z * c_3^z < 0 < (c_6^z)^2$, the solutions, the band crossing points, form a hyperbola in the $k_y = 0$ plane.

Since the existence of nontrivial boundary states is a hallmark of TNLSs, we have calculated the surface states of 3D LaCl by constructing the Green's functions based on the MLWF method, as shown in Fig. 3(a). It is obvious that the nontrivial drumhead-like surface states can be found in the bulk band gap, which confirms that 3D LaCl is a TNLS clearly. The drumhead-like surface states should be easily observed in the future experiments, such as angle-resolved photoelectron spectroscopy (ARPES) or scanning tunnel microscope (STM).

D. Large-gap 2D QAHI in GdX

Although GdX share the same hexagonal structure as LaX, the ground magnetic state of GdX is FM2, as discussed above, which results in different electronic structures in GdX. GdX have almost the same results, and thus, we choose GdCl as an example in the following illustration. The band structure of single-layer GdCl without SOC is shown in Fig. 2(c), which shows a similar dispersion to single-layer LaCl at a quick glance. However, unlike the single-layer LaCl, the nodal line circled around Γ point is fully gapped out in the presence of

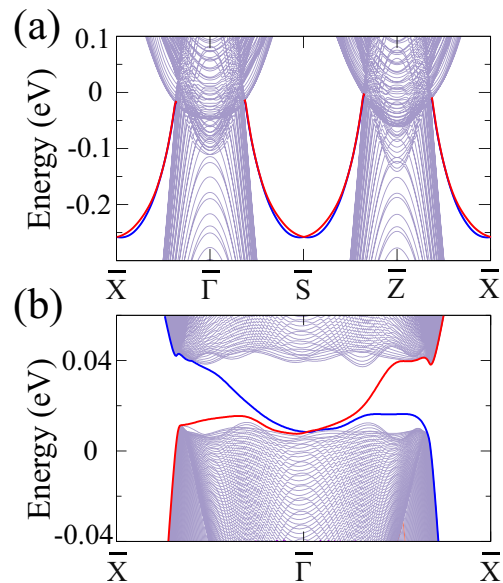


FIG. 3. (Color online) Boundary states. (a) The surface states of 3D LaCl in the (010) plane. (b) The edge states of single-layer GdCl. The red and blue bands represent the boundary states located at opposite boundaries.

SOC, as shown in the upper insets of Fig. 2(c). In spite of the unbroken threefold rotation symmetry \hat{C}_3^z , the magnetic order (FM2) breaks the mirror symmetry \hat{M}_y , which means that the nodal line loses the protection and is gapped out with a large band gap (39.4 meV and 61 meV for single-layer GdCl and single-layer GdBr, respectively).

The band gap opening at the nodal line always induce topological nontrivial phase, which can be identified by the calculation of the evolution of Wannier charge centers (WCC), as shown in Fig. 2(f). It is clearly shown that single-layer GdCl is a QAHI with Chern number $C = -1$. Furthermore, based on the MLWF method, we carry out the calculation of the edge states, as shown in Fig. 3(b), in which each edge contains a topologically protected chiral edge state in the bulk band gap. Therefore, single-layer GdCl is a large-gap 2D QAHI. When a 2D QAHI is stacked into a 3D material, the 3D material can evolve into two different nontrivial phases according to the interlayer coupling strength: 3D QAHI and Chern semimetal also called Weyl semimetal (see more details in the Appendix D). Our calculations show that 3D GdCl is a 3D QAHI due to the extremely weak interlayer binding energy. Compared with the well-known Chern semimetal, 3D QAHI is studied very few due to very rare candidates. So 3D GdCl provides an ideal platform for future study.

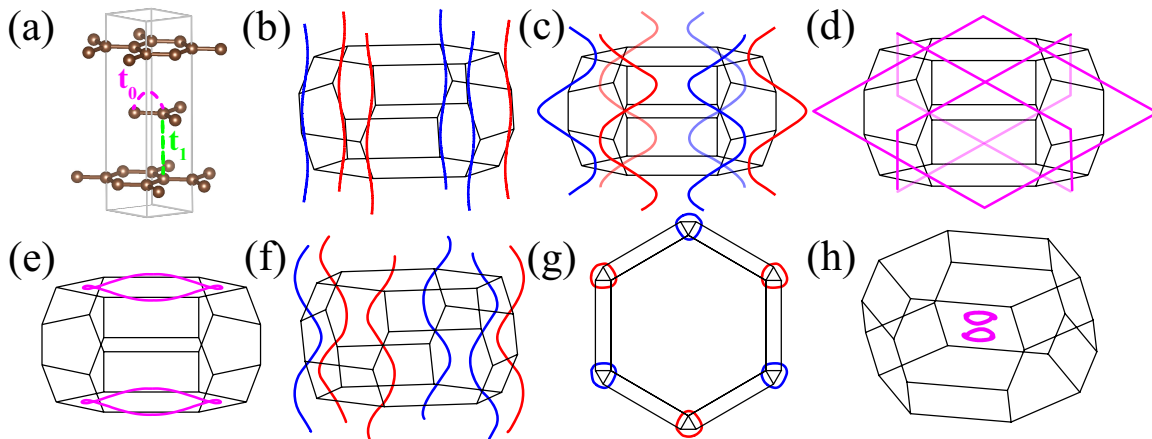


FIG. 4. (Color online) (a) The crystal structure of the ABC-stacked graphene. t_0 and t_1 are the nearest intralayer and interlayer hoppings, respectively. (b-e) The evolution of the nodal lines with different t_1/t_0 : (b) $t_1/t_0 = 0.1$, (c) $t_1/t_0 = 0.9$, (d) $t_1/t_0 = 1$, (e) $t_1/t_0 = 1.5$. (f-h) The nodal lines in the ABC-stacked graphene calculated by first-principles method. (f, g) The side view and top view of the nodal lines in the ABC-stacked graphene with interlayer distance 2.53 Å, respectively. (h) The nodal lines in the ABC-stacked graphene with interlayer distance 1.63 Å.

IV. CONCLUSION

To summarize, we show that it is much desirable to realize spinful nodal lines in 3D layered materials constructed by stacking 2D Weyl semimetals. Following this methodology as a guideline, we propose that fruitful topological phases can be found in layered ferromagnetic LnX by using the first-principles calculations and effective model analysis. More specifically, 3D LaX exhibit the long perceived spinful nodal lines extending through the whole BZ, which are protected by mirror symmetry \hat{M}_y . The spinful nodal lines appearing in pairs are fairly robust against SOC and can only be removed by moving them together in the momentum space, which is totally different from the existing nodal lines. In addition, 3D GdX, single-layer LaX and single-layer GdX are rare 3D QAHs, ideal 2D Weyl semimetals and large-gap 2D QAHs, respectively. The topological phases in LnX open a new path to realize exotic fermions, especially the nodal-line fermions, and to explore many novel properties.

ACKNOWLEDGMENTS

The authors thank Quansheng Wu, Zhijun Wang and Zhida Song for useful discussions. F. B. P. and S. N. were supported by Stanford Energy 3.0. H. W. was supported by the National Key Research and Development Program of China under grant No. 2016YFA0300600, and NSFC under grant number 11421092.

Appendix A: Nodal lines in layered materials

In order to clearly illustrate the evolution of band crossings from 2D to 3D systems, we choose an ABC-stacked graphene as an example containing two inequivalent sublattices with only one p_z -type orbital for each sublattice, as shown in Fig. 4(a). To simplify our illustration, only the nearest intralayer (t_0) and interlayer hoppings (t_1) have been taken into consideration, and a 2×2 Slater-Koster⁶⁹ tight-binding (TB) model under the crystal symmetry restrictions can be written down as follows:

$$H(\mathbf{k}) = \begin{pmatrix} 0 & t_0\delta(\mathbf{k}) + t_1\lambda(\mathbf{k}) \\ * & 0 \end{pmatrix} \quad (\text{A1})$$

where $\delta(\mathbf{k}) = e^{2\pi i(\frac{1}{3}k_x + \frac{1}{3}k_y - \frac{2}{3}k_z)} + e^{2\pi i(\frac{1}{3}k_x - \frac{2}{3}k_y + \frac{1}{3}k_z)} + e^{2\pi i(-\frac{2}{3}k_x + \frac{1}{3}k_y + \frac{1}{3}k_z)}$, $\lambda(\mathbf{k}) = e^{2\pi i(\frac{1}{3}k_x + \frac{1}{3}k_y + \frac{1}{3}k_z)}$. $k_{x,y,z}$ are defined with respect to the reciprocal lattice vectors.

It is well known that there are two band crossings at the Fermi level in the momentum space of graphene⁷⁰, which are protected by space inversion \hat{I} and time reversal (\mathcal{T}) symmetries and constrained at \mathbf{K} and \mathbf{K}' points respectively by threefold rotation symmetry about the z -axis (\hat{C}_3^z). When 2D graphene layers are stacked in an ABC-type pattern and the interlayer coupling is very weak ($t_1/t_0 = 0.1$), the band crossing points located at \mathbf{K} and \mathbf{K}' points evolve into two extended nodal lines, respectively, as shown in Fig. 4(b). As discussed in the main text, the nodal lines can only be annihilated when they meet in the momentum space, which can be easily seen by increasing the interlayer coupling strength. When $t_1/t_0 = 0.9$, the nodal lines are bended greatly and nearly touch each other, as shown in Fig. 4(c). At the critical point ($t_1/t_0 = 1$), the nodal lines connect

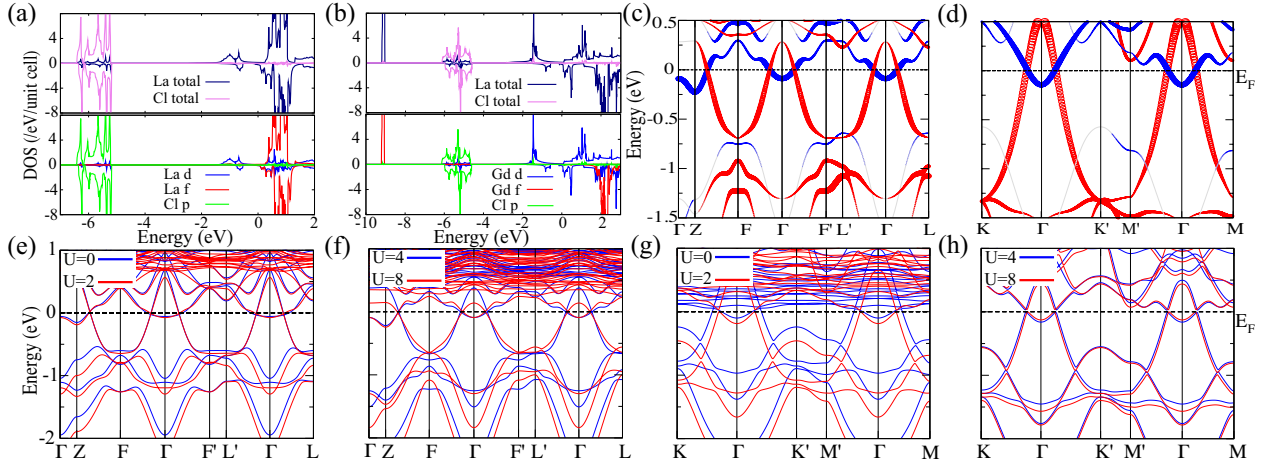


FIG. 5. (Color online) The LDA+U-calculated projected density of states of 3D LaCl (a) and 2D GdCl (b). The fatted band structures of 3D LaCl (c) and 2D GdCl (d) by LDA+U calculations. The blue and red dots represent the weights of Ln $|d_{z^2}\rangle$ and $|d_{x^2-y^2}\rangle + |d_{xy}\rangle$, respectively. The LDA+U+SOC band structures of 3D LaCl (e, f) and 2D GdCl (g, h).

with each other and become a nodal chain²⁰, as shown in Fig. 4(d). If we continue to increase t_1/t_0 to 1.5, the nodal chain becomes a closed nodal line, as shown in Fig. 4(e). The closed nodal line can be gapped out when $t_1/t_0 = 3$. Therefore, the nodal lines in the layered materials are very robust, and it is much promising to search for the TNLSs in this kind of materials.

In order to check whether this simple TB model can capture the main physics of the evolution, we have calculated the electronic structures of the ABC-stacked graphene by the first-principles method, as shown in Fig. 4(f-h). When the interlayer distance equals to 3 Å, we get two nearly straight nodal lines, which are similar to the results in Fig. 4(b). Then we decrease the interlayer distance to increase the interlayer binding strength. When the interlayer distance equals to 2.53 Å, the straight nodal lines are bended spirally, as shown in Fig. 4(f). If we view the nodal lines along z -direction (top view), the nodal lines form a ring circled around \mathbf{K} and \mathbf{K}' points, respectively, as shown in Fig. 4(g). The size of the rings has a monotonically increasing relationship with the interlayer coupling strength. At certain interlayer distance the two nodal lines touch each other, and the extended lines become closed lines in the BZ after the critical point. As shown in Fig. 4(h), there are two closed nodal lines in the BZ when the interlayer distance equals to 1.63 Å. Although the number of the closed nodal lines are not equal to the results obtained from the TB model, the evolution of the nodal lines calculated by the TB and first-principles methods are qualitatively similar.

Appendix B: Magnetic configurations and total energy calculations in LnX

Considering the partial occupations of localized orbitals of Ln, we propose four different collinear magnetic structures (FM1, FM2, AFM1, and AFM2) of LnX, as shown in Fig. 1b. As we can see, the magnetic moments of collinear FM1/AFM1 and FM2/AFM2 are aligned along the y - and the z -directions, respectively. Then, the first-principles total energy calculations are performed based on the four magnetic structures, and the results are shown in Table I, which clearly indicates that single-layer LnX have the same ground states as that of 3D LnX. To be specific, the total energies of the AFM states are about 19, 27, 138, and 198 meV/u.c. higher than that of the FM states for LaCl, LaBr, GdCl and GdBr, respectively. Moreover, although the FM states have very close total energies, LaX and GdX prefer different FM states, *i.e.* FM1, and FM2, respectively. For 3D LaCl/3D LaBr (single-layer LaCl/single-layer LaBr), FM1 states further lower the total energy about 2.09/1.52 meV/u.c. (1.94/1.61 meV/u.c.) compared with the FM2 states, while the total energies of FM2 states are about 0.72/1.08 meV/u.c. (0.78/0.99 meV/u.c.) lower than that of FM1 states for 3D GdCl/3D GdBr (single-layer GdCl/single-layer GdBr). As discussed in the main text, the different magnetic orders break different crystal symmetries and give rise to fruitful topological nontrivial phases in LnX.

Appendix C: Electronic structures of LnX

The projected density of states of 3D LaCl and 2D GdCl calculated by LDA+U are shown in Fig. 5(a) and

TABLE I. The converged total energies (unit: eV) of four different magnetic structures (FM1, FM2, AFM1, and AFM2) for LnX.

| Config. | 3D LaCl | 2D LaCl | 3D LaBr | 2D LaBr | 3D GdCl | 2D GdCl | 3D GdBr | 2D GdBr |
|---------|-----------|-----------|-----------|-----------|-----------|-----------|-----------|-----------|
| FM1 | -16.63271 | -16.51641 | -14.77393 | -14.70523 | -38.71503 | -38.76298 | -37.40773 | -37.42195 |
| FM2 | -16.63062 | -16.51447 | -14.77241 | -14.70362 | -38.71575 | -38.76376 | -37.40881 | -37.42294 |
| AFM1 | -16.61171 | -16.49404 | -14.74455 | -14.67597 | -38.57725 | -38.62517 | -37.21060 | -37.22607 |
| AFM2 | -16.60992 | -16.49223 | -14.74311 | -14.67425 | -38.57707 | -38.62562 | -37.21102 | -37.22683 |

5(b), respectively. As we can see, Cl p orbitals of 3D LaCl and 2D GdCl are mainly contributed to the states in the energy intervals (-6.5 eV to -5.1 eV) and (-6.2 eV to -4.6), respectively. La f orbitals are unoccupied for both spin up and spin down channels, while the spin up components of Gd f orbitals are fully occupied and locate from -9.2 eV to -9.1 eV. For the bands around the Fermi level (0 eV), it is clearly shown that they are dominated by the Ln d and Ln f orbitals. In order to get detail orbital character of the crossing bands, we performed the fatted band structure calculations, as shown in Fig. 5(c) and 5(d). As pointed out in the main text, the point group of nonmagnetic LnX is D_{3d} , five degenerate d orbitals in the trigonal field effect are split into one singlet (d_{z^2}) and two doublets (one is $d_{x^2-y^2}$ and d_{xy} , and the other one is d_{xz} and d_{yz}). It is obvious that there exists an obvious weight exchange near the Fermi level and the two crossing bands are dominated by Ln $|d_{z^2}\rangle$ and $|d_{x^2-y^2}\rangle + |d_{xy}\rangle$, whose weights are represented by the size of the blue and red dots, respectively. By combining these atomic orbitals, the explicit form of the two low-energy states can be written down as $r_1(|Ln_1d_{z^2}\rangle - |Ln_2d_{z^2}\rangle)$ and a combination of $r_2(|Ln_1d_{x^2-y^2}\rangle - |Ln_2d_{x^2-y^2}\rangle)$ and $r_3(|Ln_1d_{xy}\rangle - |Ln_2d_{xy}\rangle)$, where r_1 , r_2 and r_3 are material-dependent coefficients. For example, for 3D LaCl, r_1 , r_2 and r_3 equal to 0.359, 0.342 and 0.342, respectively.

In addition, the nontrivial properties of 3D LaCl and 2D GdCl are checked with different U, which are shown in Fig. 5(e), 5(f), 5(g) and 5(h). By increasing U, the depth of the band inversion at Γ point decreases monotonously for both 3D LaCl and 2D GdCl. However, the nodal lines in 3D LaCl and QAHI in 2D GdCl can still be found when $U = 8$ eV. Therefore, it is very promising to find these nontrivial phases in ferromagnetic LnX.

Appendix D: 3D QAHI and Chern semimetal

2D QAHI characterized by nonzero Chern number and quantized Hall conductance exhibits robust dissipationless chiral edge states in the bulk band gap, as shown in

Fig. 6(a). As discussed in the main text, the 3D material constructed by stacking the 2D QAHI with $C=1$ may evolve into two different topological nontrivial phases, including 3D QAHI and Chern semimetal (also called Weyl semimetal), as shown in Fig. 6(b) and 6(c), respectively. When the interlayer binding strength is very weak, the 3D material is a 3D QAHI with $C = 1$ for all

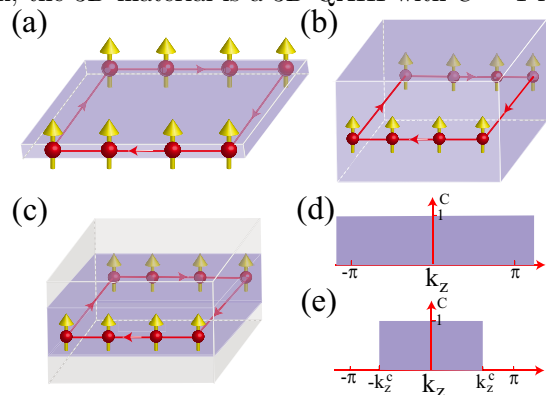


FIG. 6. (Color online) (a, b, c) Schematics of 2D QAHI, 3D QAHI and Chern semimetal, respectively. (d, e) The Chern number C as function of k_z for 3D QAHI and Chern semimetal, respectively.

k_x -, k_y - or k_z -fixed planes in the 3D BZ, which is consistent with previous result⁴⁴. To be specific, we choose k_z -fixed planes as examples for the illustration, as shown in Fig. 6(d). For 3D material with strong interlayer binding strength (Chern semimetal), the Chern number equals to 1 for the plane with $-k_z^c < k_z < k_z^c$, and equals to 0 for the plane with $-\pi < k_z < -k_z^c$ or $k_z^c < k_z < \pi$, as shown in 6(e). At the critical plane with $k_z = -k_z^c$ ($k_z = k_z^c$), there is a Weyl node with chiral charge 1 (-1). Although the Chern semimetal has been well studied⁴², the research on 3D QAHI is very few owing to the lack of promising candidates. Therefore, 3D GdX without trivial pocket will greatly facilitate the research on the nontrivial properties in 3D QAHI.

* smnie@stanford.edu

¹ A. Burkov, M. Hook, and L. Balents, Physical Review B

84, 235126 (2011).

² C. Fang, Y. Chen, H.-Y. Kee, and L. Fu, Physical Review

- B **92**, 081201 (2015).
- ³ H. Weng, X. Dai, and Z. Fang, *J. Phys.: Condens. Matter* **28**, 303001 (2016).
 - ⁴ S. M. Young, S. Zaheer, J. C. Teo, C. L. Kane, E. J. Mele, and A. M. Rappe, *Physical review letters* **108**, 140405 (2012).
 - ⁵ Z. Wang, Y. Sun, X.-Q. Chen, C. Franchini, G. Xu, H. Weng, X. Dai, and Z. Fang, *Physical Review B* **85**, 195320 (2012).
 - ⁶ Z. Wang, H. Weng, Q. Wu, X. Dai, and Z. Fang, *Physical Review B* **88**, 125427 (2013).
 - ⁷ H. B. Nielsen and M. Ninomiya, *Physics Letters B* **130**, 389 (1983).
 - ⁸ X. Wan, A. M. Turner, A. Vishwanath, and S. Y. Savrasov, *Physical Review B* **83**, 205101 (2011).
 - ⁹ L. Balents, *Physics A*, 36 (2011).
 - ¹⁰ R. Yu, Q. Wu, Z. Fang, and H. Weng, *Phys. Rev. Lett.* **119**, 036401 (2017).
 - ¹¹ Y. Du, X. Bo, D. Wang, E.-j. Kan, C.-G. Duan, S. Y. Savrasov, and X. Wan, arXiv preprint arXiv:1708.04556 (2017).
 - ¹² Y. Kim, B. J. Wieder, C. Kane, and A. M. Rappe, *Physical review letters* **115**, 036806 (2015).
 - ¹³ R. Yu, H. Weng, Z. Fang, X. Dai, and X. Hu, *Physical review letters* **115**, 036807 (2015).
 - ¹⁴ J.-M. Carter, V. V. Shankar, M. A. Zeb, and H.-Y. Kee, *Phys. Rev. B* **85**, 115105 (2012).
 - ¹⁵ S. Nie, G. Xu, F. B. Prinz, and S.-c. Zhang, *Proceedings of the National Academy of Sciences* **114**, 10596 (2017).
 - ¹⁶ K. Dolui, S. Ray, and T. Das, *Phys. Rev. B* **92**, 205133 (2015).
 - ¹⁷ M. Wu, *2D Materials* **4**, 021014 (2017).
 - ¹⁸ J.-T. Wang, H. Weng, S. Nie, Z. Fang, Y. Kawazoe, and C. Chen, *Physical review letters* **116**, 195501 (2016).
 - ¹⁹ Y. Chen, Y. Xie, S. A. Yang, H. Pan, F. Zhang, M. L. Cohen, and S. Zhang, *Nano letters* **15**, 6974 (2015).
 - ²⁰ T. Bzdušek, Q. Wu, A. Rüegg, M. Sigrist, and A. A. Soluyanov, *Nature* **538**, 75 (2016).
 - ²¹ N. B. Kopnin, T. T. Heikkilä, and G. E. Volovik, *Phys. Rev. B* **83**, 220503 (2011).
 - ²² G. Volovik, *Physica Scripta* **2015**, 014014 (2015).
 - ²³ T. T. Heikkilä and G. E. Volovik, in *Basic Physics of Functionalized Graphite* (Springer, 2016) pp. 123–143.
 - ²⁴ J.-W. Rhim and Y. B. Kim, *Physical Review B* **92**, 045126 (2015).
 - ²⁵ Y. Huh, E.-G. Moon, and Y. B. Kim, *Physical Review B* **93**, 035138 (2016).
 - ²⁶ H. Weng, Y. Liang, Q. Xu, R. Yu, Z. Fang, X. Dai, and Y. Kawazoe, *Phys. Rev. B* **92**, 045108 (2015).
 - ²⁷ L. S. Xie, L. M. Schoop, E. M. Seibel, Q. D. Gibson, W. Xie, and R. J. Cava, *Apl Materials* **3**, 083602 (2015).
 - ²⁸ Y.-H. Chan, C.-K. Chiu, M. Chou, and A. P. Schnyder, *Physical Review B* **93**, 205132 (2016).
 - ²⁹ M. Hirayama, R. Okugawa, T. Miyake, and S. Murakami, *Nature communications* **8** (2017).
 - ³⁰ J. Zhao, R. Yu, H. Weng, and Z. Fang, *Phys. Rev. B* **94**, 195104 (2016).
 - ³¹ Q. Xu, R. Yu, Z. Fang, X. Dai, and H. Weng, *Phys. Rev. B* **95**, 045136 (2017).
 - ³² T.-R. Chang, I. Pletikoscic, T. Kong, G. Bian, A. Huang, J. Denlinger, S. K. Kushwaha, B. Sinkovic, H.-T. Jeng, T. Valla, W. Xie, and R. J. Cava, arXiv preprint arXiv:1711.09167 (2017).
 - ³³ X. Feng, C. Yue, Z. Song, Q. Wu, and B. Wen, *Physical Review Materials* **2**, 014202 (2018).
 - ³⁴ J.-T. Wang, S. Nie, H. Weng, Y. Kawazoe, and C. Chen, *Physical Review Letters* **120**, 026402 (2018).
 - ³⁵ R. Li, H. Ma, X. Cheng, S. Wang, D. Li, Z. Zhang, Y. Li, and X.-Q. Chen, *Physical review letters* **117**, 096401 (2016).
 - ³⁶ Y. Chen, Y.-M. Lu, and H.-Y. Kee, *Nature communications* **6** (2015).
 - ³⁷ G. Bian, T.-R. Chang, R. Sankar, S.-Y. Xu, H. Zheng, T. Neupert, C.-K. Chiu, S.-M. Huang, G. Chang, I. Belopolski, D. S. Sanchez, M. Neupane, N. Alidoust, C. Liu, B. Wang, C.-C. Lee, H.-T. Jeng, C. Zhang, Z. Yuan, S. Jia, A. Bansil, F. Chou, H. Lin, and M. Z. Hasan, *Nature communications* **7**, 10556 (2016).
 - ³⁸ L. M. Schoop, M. N. Ali, C. Straßer, A. Topp, A. Varykhalov, D. Marchenko, V. Duppel, S. S. Parkin, B. V. Lotsch, and C. R. Ast, *Nature communications* **7** (2016).
 - ³⁹ B. Fu, C. Yi, T. Zhang, M. Caputo, J. Ma, X. Gao, B. Lv, L. Kong, Y. Huang, M. Shi, S. Vladimir, C. Fang, H. Weng, Y. Shi, T. Qian, and H. Ding, arXiv preprint arXiv:1712.00782 (2017).
 - ⁴⁰ R. Yu, W. Zhang, H.-J. Zhang, S.-C. Zhang, X. Dai, and Z. Fang, *Science* **329**, 61 (2010).
 - ⁴¹ H. Zhang, J. Wang, G. Xu, Y. Xu, and S.-C. Zhang, *Phys. Rev. Lett.* **112**, 096804 (2014).
 - ⁴² G. Xu, H. Weng, Z. Wang, X. Dai, and Z. Fang, *Physical review letters* **107**, 186806 (2011).
 - ⁴³ C.-Z. Chang, J. Zhang, X. Feng, J. Shen, Z. Zhang, M. Guo, K. Li, Y. Ou, P. Wei, L.-L. Wang, Z.-Q. Ji, Y. Feng, S. Ji, X. Chen, J. Jia, X. Dai, Z. Fang, S.-C. Zhang, K. He, Y. Wang, L. Lu, X.-C. Ma, and Q.-K. Xue, *Science* **340**, 167 (2013).
 - ⁴⁴ B. I. Halperin, *Japanese Journal of Applied Physics* **26**, 1913 (1987).
 - ⁴⁵ T. Hyart, R. Ojajarvi, and T. Heikkilä, arXiv preprint arXiv:1709.05265 (2017).
 - ⁴⁶ P. Blaha, K. Schwarz, G. Madsen, D. Kvasnicka, and J. Luitz, WIEN2k, An Augmented Plane Wave Plus Local Orbitals Program for Calculating Crystal Properties (TU Vienna, Vienna, 2001).
 - ⁴⁷ G. Kresse and J. Furthmüller, *Computational materials science* **6**, 15 (1996).
 - ⁴⁸ G. Kresse and J. Furthmüller, *Physical review B* **54**, 11169 (1996).
 - ⁴⁹ J. P. Perdew and Y. Wang, *Phys. Rev. B* **45**, 13244 (1992).
 - ⁵⁰ A. Liechtenstein, V. Anisimov, and J. Zaanen, *Physical Review B* **52**, R5467 (1995).
 - ⁵¹ N. Marzari, A. A. Mostofi, J. R. Yates, I. Souza, and D. Vanderbilt, *Reviews of Modern Physics* **84**, 1419 (2012).
 - ⁵² M. L. Sancho, J. L. Sancho, and J. Rubio, *Journal of Physics F: Metal Physics* **14**, 1205 (1984).
 - ⁵³ M. L. Sancho, J. L. Sancho, J. L. Sancho, and J. Rubio, *Journal of Physics F: Metal Physics* **15**, 851 (1985).
 - ⁵⁴ Q. Wu, S. Zhang, H.-F. Song, M. Troyer, and A. A. Soluyanov, *Computer Physics Communications* **224**, 405 (2018).
 - ⁵⁵ C. L. Kane and E. J. Mele, *Physical review letters* **95**, 226801 (2005).
 - ⁵⁶ B. A. Bernevig, T. L. Hughes, and S.-C. Zhang, *Science* **314**, 1757 (2006).
 - ⁵⁷ M. König, S. Wiedmann, C. Brüne, A. Roth, H. Buhmann, L. W. Molenkamp, X.-L. Qi, and S.-C. Zhang, *Science* **318**, 766 (2007).

- ⁵⁸ L. Fu, C. L. Kane, and E. J. Mele, *Physical review letters* **98**, 106803 (2007).
- ⁵⁹ H. B. Nielsen and M. Ninomiya, *Nuclear Physics B* **185**, 20 (1981).
- ⁶⁰ H. B. Nielsen and M. Ninomiya, *Nuclear Physics B* **193**, 173 (1981).
- ⁶¹ C. Fang and L. Fu, *Physical Review B* **91**, 161105 (2015).
- ⁶² K. Shiozaki, M. Sato, and K. Gomi, *Physical Review B* **91**, 155120 (2015).
- ⁶³ C. Fang and L. Fu, *arXiv preprint arXiv:1709.01929* (2017).
- ⁶⁴ R. E. Araujo and J. D. Corbett, *Inorganic Chemistry* **20**, 3082 (1981).
- ⁶⁵ H. Mattausch, A. Simon, N. Holzer, and R. Eger, *Zeitschrift für anorganische und allgemeine Chemie* **466**, 7 (1980).
- ⁶⁶ H. Weng, X. Dai, and Z. Fang, *Physical review X* **4**, 011002 (2014).
- ⁶⁷ M. Dion, *Phys. Rev. Lett.* **92**, 246401 (2004).
- ⁶⁸ C. Gong, L. Li, Z. Li, H. Ji, A. Stern, Y. Xia, T. Cao, W. Bao, C. Wang, Y. Wang, Z. Q. Qiu, R. J. Cava, S. G. Louie, J. Xia, and X. Zhang, *Nature* (2017).
- ⁶⁹ J. C. Slater and G. F. Koster, *Phys. Rev.* **94**, 1498 (1954).
- ⁷⁰ S. D. Sarma, S. Adam, E. Hwang, and E. Rossi, *Reviews of Modern Physics* **83**, 407 (2011).